https://doi.org/10.5194/egusphere-2026-3996
Preprint. Discussion started: 2 September 2026

Discretized thermodynamic imaging for the measurement of precipitation and winds

Timothy J. Garrett[1], Ryan Szczerbinski[1], Eric R. Pardyjak[2], Dhiraj K. Singh[2], Allan T. Reaburn[3], Benjamin H. Silberman[2], Karlie N. Rees[1], and Alexander Blackmer[1]

[1]Department of Atmospheric Sciences, University of Utah, Salt Lake City, UT, USA
[2]Department of Mechanical Engineering, University of Utah, Salt Lake City, UT, USA
[3]Particle Flux Analytics Inc., Park City, UT, USA

Correspondence: Timothy J. Garrett (tim.garrett@utah.edu)

Abstract. Precipitation and winds impart spatially and temporally variable thermodynamic signatures on surfaces. Here, we describe two new hotplate sensors, the DTI-pm and DTI-de, that sample energy flows using a discretized thermodynamic imaging (DTI) principle. Unlike prior single-element hotplate devices, DTI measurements are obtained at sufficiently high spatial resolution to separate component thermodynamic signatures. The DTI-pm is a sensor array of individually controlled micro-hotplates, each using pulse-width modulation to maintain a constant elevated temperature of each sensor element, measuring the power required to do so. The DTI-de uses an infrared camera that passively monitors radiative temperatures on a heated metal plate by exploiting the differential emissivity between metal and water; heat transfer physics is used to infer the power of thermodynamic cooling. Both techniques are shown here to be capable of measuring with exceptionally high accuracy and precision a wide range of precipitation characteristics, including mass, size, and the density of individual multi-phase hydrometeors, as well as continuous bulk precipitation rates and snow density. The DTI-de achieves a spatial resolution of 0.2 mm with a mass sensitivity of 1 μg, while the DTI-pm provides a spatial resolution of 1 mm and a mass sensitivity of 0.5 μg. Preliminary results suggest the potential for the DTI-pm and DTI-de to concurrently measure wind speed and direction.

1 Introduction

There is a rapidly growing societal need for real-time, observation-based tools that account for the extremely high spatial and temporal variability of precipitation-related variables. Hydrological intensification with climate warming (Huntington, 2010; Kirchmeier-Young and Zhang, 2020) is straining existing water management infrastructure (Ficklin et al., 2022), impacting agricultural systems (Huntington, 2010), and leading to loss of life (Nanditha et al., 2023). Yet available ground-based precipitation measurement techniques struggle to meet the needed precision and accuracy (Cauteruccio et al., 2021). In fact, the gold standard for modern liquid precipitation measurement remains a tipping-bucket gauge (Kidd et al., 2017), a design that was first conceived three and a half centuries ago by the English architects and polymaths Sir Christopher Wren and Robert Hooke

https://doi.org/10.5194/egusphere-2026-3996
Preprint. Discussion started: 2 September 2026

between 1662 and 1679 (Biswas, 1967). Weighing gauges provide an alternative method for determining precipitation mass from gravitational pressure that is better suited for the measurement of solid precipitation (Goodison et al., 1998). However, both designs face the challenge of frequent maintenance needs and poor catchment efficiency, particularly during high winds (Jevons, 1861; Goodison et al., 1998; Tapiador et al., 2012; Thériault et al., 2012; Thériault et al., 2021).

Some of these collection concerns can be avoided by using optical gauges that determine precipitation rate from the occlusion or scattering of a light beam by individual particles. Among the more advanced and popular probes is the Parsivel^2 disdrometer (Löffler-Mang et al., 1999), which infers precipitation rates by integrating a measured size distribution. It has high accuracy for measuring rain, but collection concerns remain: if wind speeds are high parallel to the beam, undercatch can be as high as 100% (Chinchella et al., 2025). Moreover, for particles that are more irregularly shaped, such as mixed-phase and frozen precipitation, no simple relationship exists between occlusion of a light beam and the requisite aspect of mass (Johannsen et al., 2020). Battaglia et al. (2010) compared falling snow observations of the Parsivel^2 against another optical disdrometer, the 2-DVD, to find that the Parsivel^2 can skew size distributions towards smaller particles: large particles may be counted as multiple small particles, and high winds can reduce the particle cross-section in the laser beam.

Hotplate technologies obtain hydrometeor mass by measuring the energy required to evaporate water. In principle the measurement assumptions are far fewer than any weighing or optical techniques because there is a linear relationship between mass and the latent heat of evaporation (Stickel et al., 2005), there are no moving parts, and there is no collection aperture (Thériault et al., 2021). While tantalizing for the potential for improved accuracy, such devices are nonetheless limited by high power requirements, maintenance issues, and a sensitivity to high winds during low precipitation rates (Rasmussen et al., 2011).

We describe here a new hotplate technique we term discretized thermal imaging (DTI) that we demonstrate as both more precise and accurate than prior precipitation measurement designs, including past hotplate attempts. Two approaches are explored, an active (DTI-pm) method that measures the energy required to maintain discretized plates at constant temperature using pulse-width modulation, and a passive method (DTI-de) that uses infrared imagery to monitor hydrometeor evaporation exploiting the different emissivities of water and metal. We outline laboratory and field measurements demonstrating high precipitation measurement precision and accuracy, and further show preliminary evidence of the suitability of the DTI-pm and DTI-de designs for concurrently measuring wind speed and direction.

2 Overview of the DTI-pm and DTI-de precipitation measurement techniques

The DTI working principle is to quantify the thermal energy transfer into an individual hydrometeor. For a hydrometeor that has fallen on a heated plate, the heat loss from the plate to the hydrometeor as it melts and evaporates can be directly related to its mass through the latent and sensible heat of water, the temperature difference between the plate and the hydrometeor, and the hydrometeor area (Bergman et al., 2011). Heat gained by a hydrometeor is equal to heat lost from the plate, in proportion to the heat flux into the particle q above any background signal, the area of the interface between the hydrometeor and the plate A, and the evaporation time δt. For the special case of snow particles, the mass of a single hydrometeor measured using the

https://doi.org/10.5194/egusphere-2026-3996
Preprint. Discussion started: 2 September 2026

DTI is then given by (Singh et al., 2021)

$$m = \frac{1}{L_{eq} + c_{ice}(T_0 - T_{ice,0}) + c_{liq}(T_p - T_0)} \int_0^{\delta t} qA dt, \quad (1)$$

where L_{eq} is the sum of the latent heats of melting and vaporization of water, c_{ice} and c_{liq} are the specific heat capacities of ice and liquid water, respectively; $T_0 = 0°\text{C}$ is the freezing temperature; $T_{\text{ice},0}$ is the initial temperature of the frozen particle; and T_p is the sensor setpoint temperature. The thermodynamic coefficients in Eq. 1 are readily adjusted for the case of rain, where melting is not part of the problem. The DTI principle relies upon measurement of the thermodynamic power $P = qA$ per discrete element so that background power fluctuations owing to wind, temperature fluctuations, and possible radiation losses can be subtracted from the hydrometeor signal. The total precipitation rate can then be determined from the sum of all hydrometeor masses measured by the senor area within a predetermined time interval. Snow Water Equivalent (SWE) rates are defined as the liquid precipitation rates of fully melted snow.

2.1 Power-modulated DTI sensing

The power-modulated DTI-pm device exploits (1) by using an array of small, upward facing heater elements integrated with a micro-hotplate control and data management system for individual plate control. By monitoring the power per pixel required to maintain a constant micro-hotplate resistance – effectively a constant temperature – a 2D temporal heat map is obtained, a "video" of atmospheric thermodynamic signatures that perturb the plate from the chosen baseline temperature.

The current DTI-pm alpha-prototype shown in Fig. 1 is a 576-sensor 24×24 array of 0.5 mm×0.5 mm micro-hotplate sensors, separated by 0.6 mm, and arranged in a footprint of 26.4 mm × 26.4 mm. Heaters are maintained at a constant elevated temperature using a pulse-width modulation (hence DTI-pm) control strategy (Foss et al., 1996) to provide a thermodynamic video with a temporal resolution of 10 Hz, and a spatial resolution of ∼1 mm, neglecting any unlikely coincidence errors when two small particles land simultaneously on adjacent plates and are sampled as one larger particle (Lance, 2012) . Conventional microfabrication techniques are used to create rasterized platinum micro-heater diaphragms, each a nominal 0.5 mm across and 3 μm thick, deposited and patterned on top of a polyamide PCB substrate (e.g. Ahmad et al., 2022). Wiring from the heaters to a micro-controller uses through-vias embedded in the PCB to connect individual platinum heaters on the top side of the PCB to contact pads on the backside. The device is calibrated by measuring of the resistance of each micro-heater.

Due to the low thermal inertial of the micro-hotplates, the DTI-pm is highly sensitive to fluctuations in ambient thermodynamic signatures. It is also capable of measuring both the areas and linear dimensions of particles larger than the nominal sensor size of 0.5 mm as well as the liquid volume-equivalent diameters of smaller particles. An added ability is to automatically engage adaptive sampling, separating a high quasi-stationary precipitation power draw from a lower, more variable wind signature. Wind speed is inferred from the summation of power increments over the sampling time and micro-hotplate array cross-section. Direction is determined from gradients across the array. Turbulence can potentially be inferred from spatio-temporal power fluctuations.

https://doi.org/10.5194/egusphere-2026-3996
Preprint. Discussion started: 2 September 2026

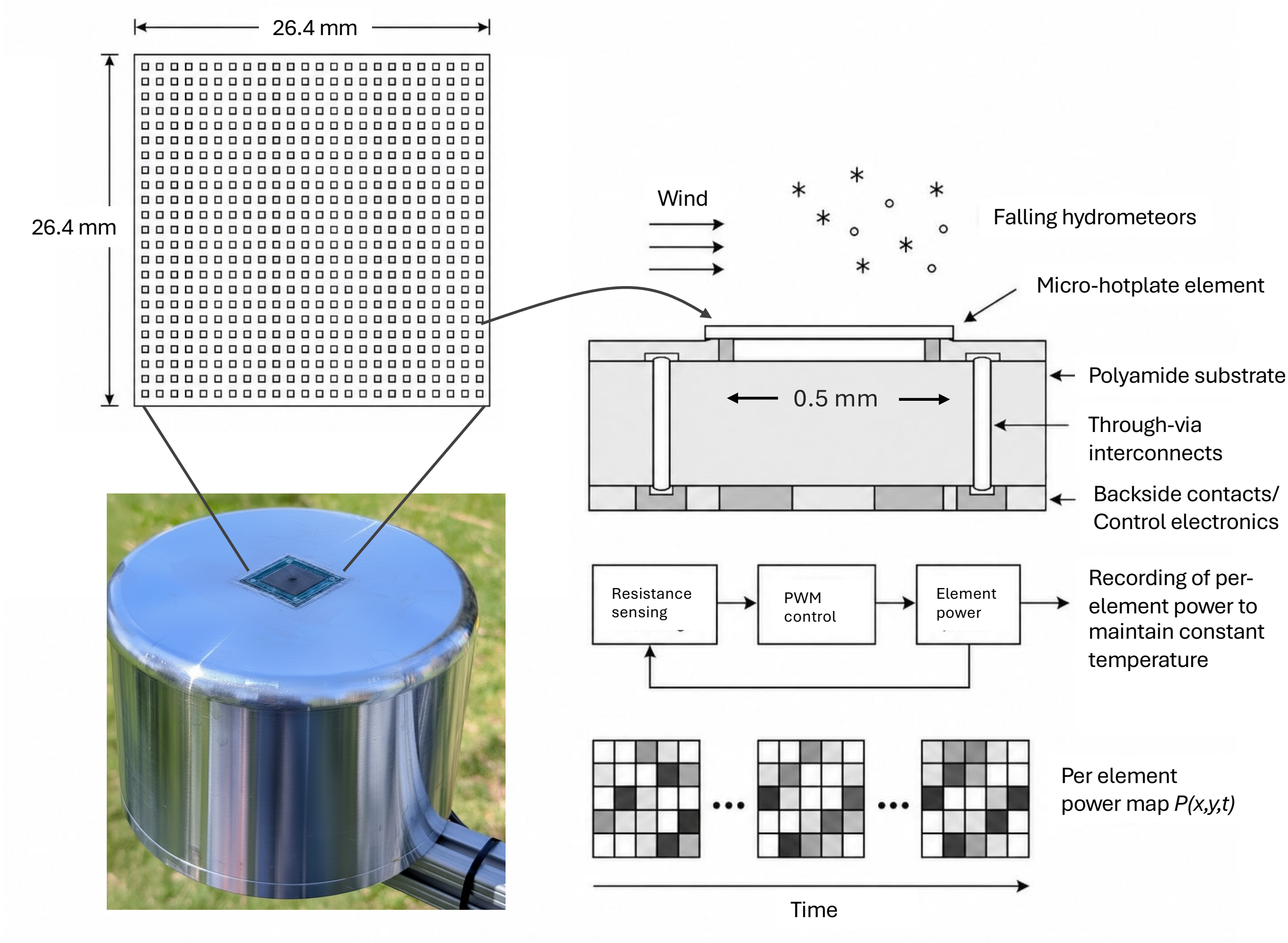

Figure 1. The DTI-pm measurement method of hydrometeor density and mass. A 24×24 array of 576 micro-hotplate sensors is maintained through pulse-width modulation at a constant temperature. The power map creates a thermodynamic "video" that is used to determine wind and hydrometeor cooling signatures.

2.2 Differential Emissivity DTI sensing

The DTI-de design (also termed the Differential Emissivity Imaging Disdrometer or DEID) has been outlined previously (Rees et al., 2021; Singh et al., 2021; Morrison et al., 2023; Singh et al., 2024). The DTI-de was initially conceived as a calibration device for the DTI-pm, and differs by maintaining a heated plate at a temperature that lies just below the Leidenfrost point. The plate is roughened to maximize heat transfer and to maintain a droplet contact angle of about 90°. Solid or liquid hydrometeors that land on the heated plate are seen by an infrared camera as high-contrast regions of interest (ROIs) (see Figure 2) due to the large difference in infrared emissivity between absorbing water and the reflective metal plate – even if the physical temperature is the same, the radiative temperature of evaporating droplets on a heated metal plate differs by ∼100 K. The

https://doi.org/10.5194/egusphere-2026-3996
Preprint. Discussion started: 2 September 2026

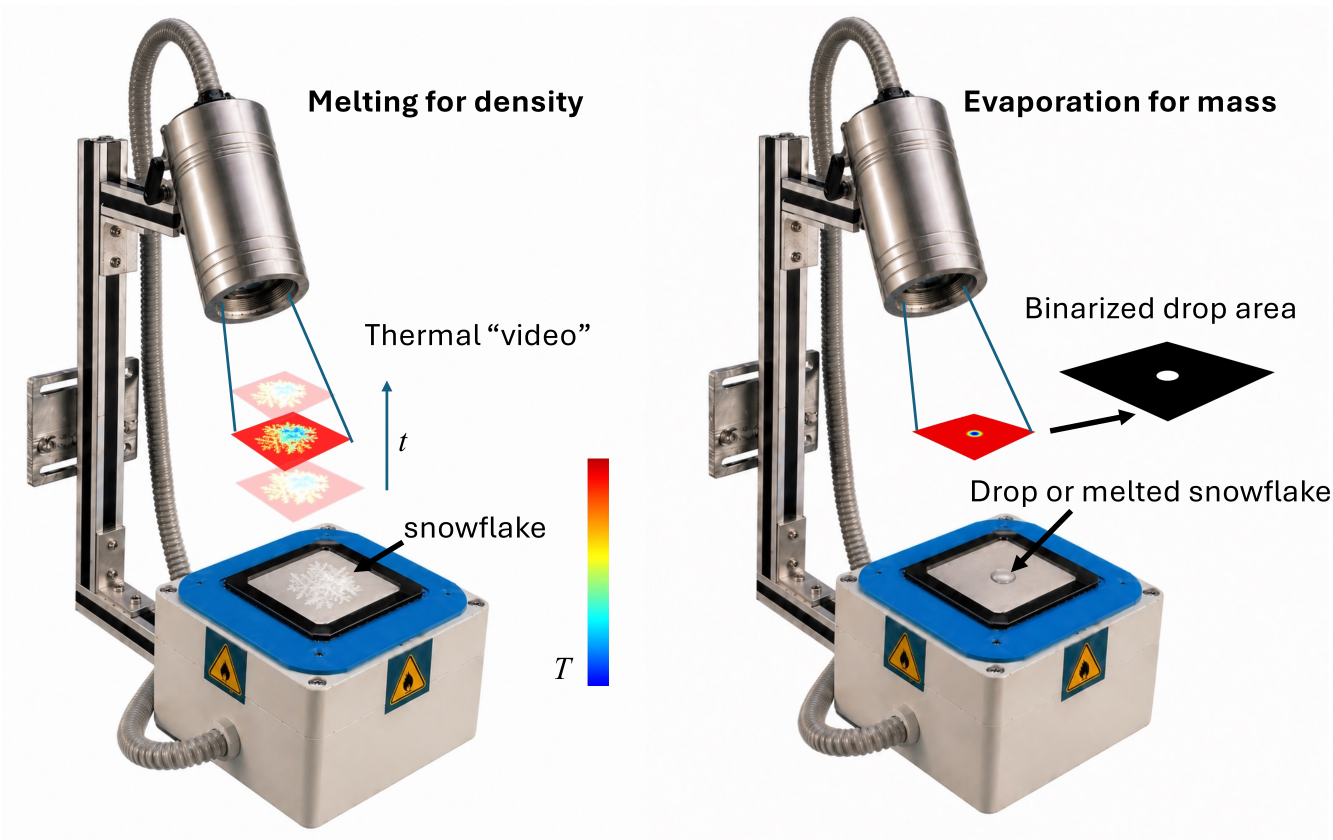

Figure 2. The DTI-de measurement method of hydrometeor density and mass (Singh et al., 2021, 2024) Left: High-emissivity snowflakes on a low-emissivity heated metal plate are imaged by an infrared camera to obtain a thermal video. Measurement of a "melting speed" dT/dt during the melting process yields snowflake density. Right: A thermal image of a melted snowflake or drop is converted to a binary image to obtain hydrometeor mass from the evaporation time and the drop area.

thermal temperature of the plate is monitored from the observed temperature of a piece of known high-emissivity Kapton tape placed on the plate edge. The thermal signature of each ROI is sampled by the camera at high frequency (15 Hz in the current design) at a nominal (and adjustable) resolution of 0.2 mm to obtain time series for hydrometeor temperature, plate temperature, area, melt time, and evaporation time. Particle mass is then obtained from (1) where q is proportional to a coefficient of heat transfer and the difference between the temperatures of the plate surface T_s and the top of the melted snowflake or evaporating droplet particle T_p, i.e. $q = \alpha \Delta T = \alpha (T_s - T_p)$. The value of α is determined through controlled laboratory experiments as described in Singh et al. (2021). Particle density is obtained by measuring the speed at which the temperature difference ΔT between the top of a frozen, unmelted particle and the plate diminishes over the course of particle melting as it equilibrates to $\Delta T = T_p$ and $T_s = 0$, what was termed a "melting speed" $v_{\mathrm{melt}} = |d\Delta T/dt|$ (Singh et al., 2024). Porous particles with low

https://doi.org/10.5194/egusphere-2026-3996
Preprint. Discussion started: 2 September 2026

thermal conductivity air gaps melt more slowly than continuous ice, meaning that the particle density is inversely related to v_{melt}.

An important advantage of the DTI principle compared with other hotplate designs is that measurements of particle mass and density are highly insensitive to fluctuating thermodynamic forcing of the plate that are distinct from the precipitation signature, most notably winds. The underlying explanation is that a thermodynamic perturbation that affects a portion of the plate that is uncovered also affects the top of the evaporating droplet. Any conceivable precipitation particle is sufficiently small that conduction and convection transmit this signature from the top of the particle to the underlying plate below. Thus, even during high wind conditions, the temperature difference between the top and bottom of the droplet ΔT remains nearly fixed, as verified in wind tunnel experiments with a high resolution thermal camera looking sideways at the evaporating particle (Singh et al., 2021).

3 Laboratory evaluation

3.1 Particle mass

Figure 3 shows an evaluation of the DTI principle for laboratory measurement of particulate mass. Deionized water droplets from a micropipette with masses ranging from 2 mg to nearly 200 mg were placed on the DTI-pm and DTI-de surfaces in a constant temperature and relative humidity environment with an open-topped square enclosure designed to minimize wind. For each trial, complete, continuous discharge of water from the pipette was ensured by placing it close to the hotplate. A linear regression through the origin of measured versus generated mass has a slope of 1.038 with 95% confidence bounds of $[0.999, 1.079]$. The largest tested drops of 120 mg covered the entire array, although these would correspond to spherical water droplets of 6 mm diameter that are unlikely to be encountered in the field (Hobbs and Rangno, 2004; Villermaux and Bossa, 2009).

Micropipettes are ill-suited for determining the lower measurement size limit. For the DTI-de, the minimum resolved mass is limited by the camera resolution of the observed plate and the density of the particle, nominally $1\,\mu$g for the device described by Singh et al. (2021). An estimate of the minimum droplet measurement sensitivity of the DTI-pm was established by directly imaging with an SLR video camera particles produced by a spray device falling through a horizontal laser sheet placed just above the array of micro-heater elements. The camera determined the number and size of particles falling through the light beam onto the array. Droplet mass was inferred assuming spherical droplet geometry and the density of liquid water. These were then compared to DTI-pm cumulative mass measurements. Values of q in Eq. 1 were calculated by subtracting the median value of each sensor. Over a ten second period the SLR camera imaged 1,254 individual water droplets with an exponential droplet size distribution ranging from 0.1 mm to 0.5 mm diameter that fell directly onto the microheater array. The SLR-calculated mean particle mass was 4.7 μg compared to the DTI-pm measured mean mass of 5.1 μg. The size corresponds to a diameter of 213 μm, characteristic of small drizzle or mist. The signal to noise ratio for the device approached unity for a measured mass corresponding to a 83 μm droplet with a mass of 0.3 μg suggesting an approximately resolution of 0.5 μg.

https://doi.org/10.5194/egusphere-2026-3996
Preprint. Discussion started: 2 September 2026

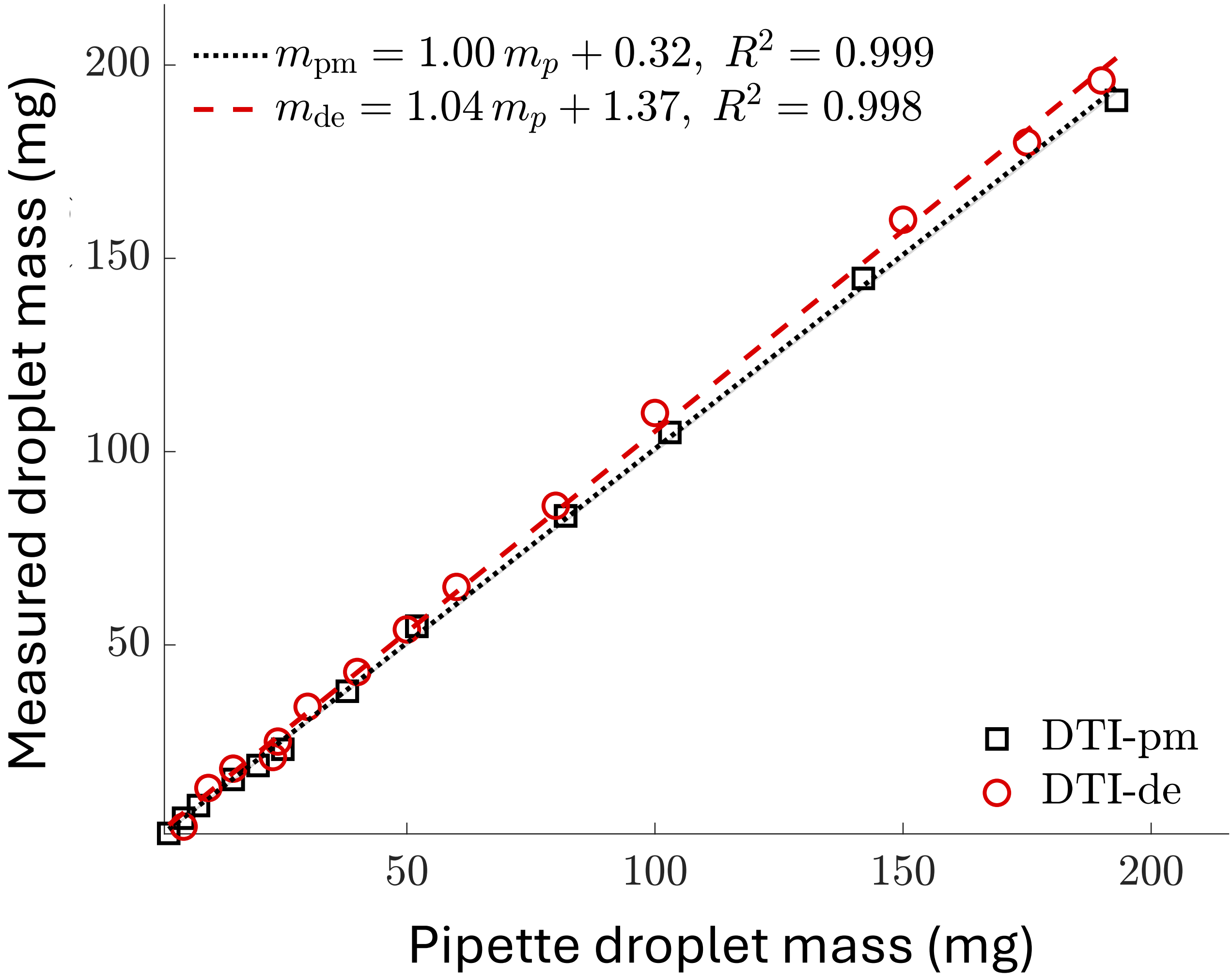

Figure 3. Correlation between water-droplet masses measured by a calibrated micropipette and those obtained using the DTI-pm and the DTI-de, with corresponding linear fits. The applied micropipette masses ranged between 2 and 193 mg for the DTI-pm and 2 and 196 mg for the DTI-de. Mass was derived using Eq. 1. The coefficients of determination are 0.999 for DTI-pm and 0.998 for DTI-de. Micropipette masses were independently validated using a gravimetric scale prior to deposition on the sensors. Experiments were laboratory based with no wind at room temperature.

https://doi.org/10.5194/egusphere-2026-3996
Preprint. Discussion started: 2 September 2026

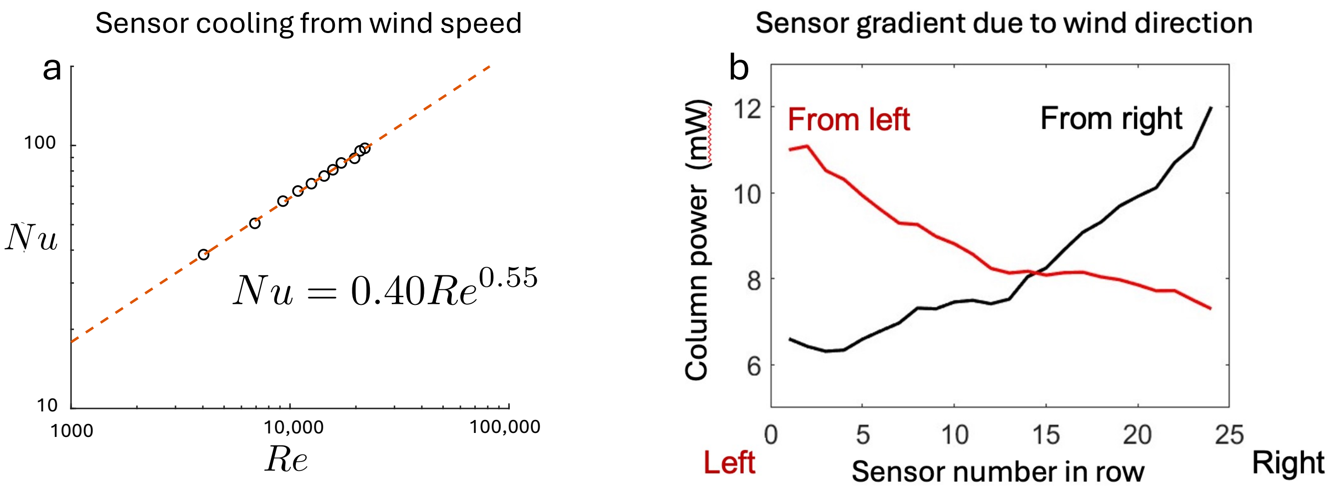

Figure 4. a) Relationship between the Nusselt and Reynolds number measured by the DTI-pm in a wind tunnel. b) Wind tunnel experiment illustrating the effect of the orientation of the wind relative to the plate on the mean power draw normal to the direction of the wind flow.

3.2 Wind speed

The array of DTI-pm sensors provides a spatial map of atmospheric thermodynamic signatures of whatever origin, and so it allows for the distinction of rapidly fluctuating wind signatures from longer-lasting stationary precipitation particles. At a basic physical level, the convective heat loss from an individual heated plate is accelerated by the flow of overlying cooler air. In principle, the average wind speed flowing over the array can be deduced from the amount of convective cooling that occurs as the plate is maintained at constant temperature (Incropera et al., 2011). The relationship between the dimensionless Nusselt number (Nu) for heat loss and the dimensionless Reynolds number (Re) characterizing the speed of the air flow, for a plate of horizontal size L that is heated above the ambient air temperature to a temperature difference ΔT while drawing electrical power P is:

$$\mathrm{Nu} = \frac{hL}{K} = \frac{P}{KL\Delta T}, \tag{2}$$

where h is the convective heat transfer coefficient, K is the thermal conductivity of air. For an air wind speed U and air kinematic viscosity ν, the Reynolds number is:

$$\mathrm{Re} = \frac{UL}{\nu} \tag{3}$$

To quantify this relationship between Nu and Re, the DTI-pm was placed in an Engineering Laboratory Design Inc. wind tunnel at the University of Utah (Singh et al., 2021). The test section where the device was placed has a 0.9 m×1.2 m cross section, maximum wind velocity of $\sim$12 m s^{-1}, and free-stream turbulence intensity $<$0.4%. The device was colocated with a pitot-static tube and 10-Torr MKS Baratron pressure transducer for measuring wind speed. The DTI-pm surface temperature

https://doi.org/10.5194/egusphere-2026-3996
Preprint. Discussion started: 2 September 2026

was maintained at $100°$ C and the wind-tunnel airflow speed was varied between $2\,\mathrm{m\,s^{-1}}$ and $12\,\mathrm{m\,s^{-1}}$ with air temperatures between $12°$ C and $23°$ C. Hot-wire and pitot-probes were used to measure the wind-tunnel speed. A power-law regression fit to the experimental data yielded the empirical relation:

$$\mathrm{Nu} = 0.40\,\mathrm{Re}^{0.55}. \quad (4)$$

While the prefactor value in Eqn. 4 is specific to the DTI-pm instrument design, the exponent value is consistent with classical forced convection theory for transitional-flow regimes: the heated element cooling scales roughly as the square root of the wind power. In general, convective heat transfer increases sublinearly with flow velocity with an exponent of 0.5 for laminar boundary layers and 0.8 for turbulent boundary layers (Çengel and Ghajar, 2015).

Figure 4b shows a strong gradient in the thermodynamic cooling signature across the thermal sensor array in the wind tunnel. The orientation depends on the direction of the air flow, with a nearly factor of two decrease in power draw from the upwind side of the array to the downwind side of the array. While these results are preliminary, the implication is that the DTI-pm has the potential to measure wind direction as well as wind speed.

A preliminary application of the DTI-de sensing technique to the measurement of wind speed is shown in Fig. 5. For this experiment, the temperature scaling of the thermal camera was switched from the standard “precipitation mode", where precipitation particles appear as bright regions on a dark background, to a more sensitive mode that reveals thermodynamic wind cooling signatures. Wind vectors on the plate were determined using a Thermal Imaging Velocimetry (TIV) technique based on the well-known 2D planar Particle Image Velocimetry (PIV) method (Raffel et al., 1998). The spatial shift of the infrared emission field from the heated DTI-de plate yields a two-dimensional velocity that can be correlated to actual wind speeds through wind tunnel calibration. The PIV technique involves breaking up interrogation regions consisting of blocks of thermal camera pixels, and then computing cross-correlation functions from temporally consecutive images. Background subtraction quickly reveals thermodynamic signatures that are stationary or slowly varying on time scales much longer than wind perturbations (e.g., melting process associated with a hydrometeors or radiation signatures). Winds are determined from the remainder. Laboratory measurements in a wind tunnel show close agreement between wind speeds of approximately $4\,\mathrm{m\,s^{-1}}$ determined with TIV using the DTI-de, and sonic anemometer measurements, agreeing to within 10%. While not described here, the rapid measurement speed of thermodynamic signatures implies a capacity to also measure levels of turbulence.

4 Field tests

We now proceed to DTI-pm and DTI-de deployments in field conditions, comparing precipitation and wind measurements to existing methods. Figure 6 illustrates DTI-pm capabilities to measure small snowflake masses during a deployment to a snow study plot at a high alpine location in Alta, Utah, located in the Wasatch Mountain Range (elevation 2,925 m, lat/lon 40.5761, -111.6389) on 19 April 2022. The total power signal shown in Figure 6a includes both wind and hydrometeor cooling signals. By itself, the trace does not allow isolation of hydrometeor power signals that would allow measurement of individual snowflake masses. Figures 6b and 6c show the thresholding procedure used to discriminate array micro-heaters that are associated with higher power output, permitting isolation of individual hydrometeor masses and diameters. The size distribution has

https://doi.org/10.5194/egusphere-2026-3996
Preprint. Discussion started: 2 September 2026

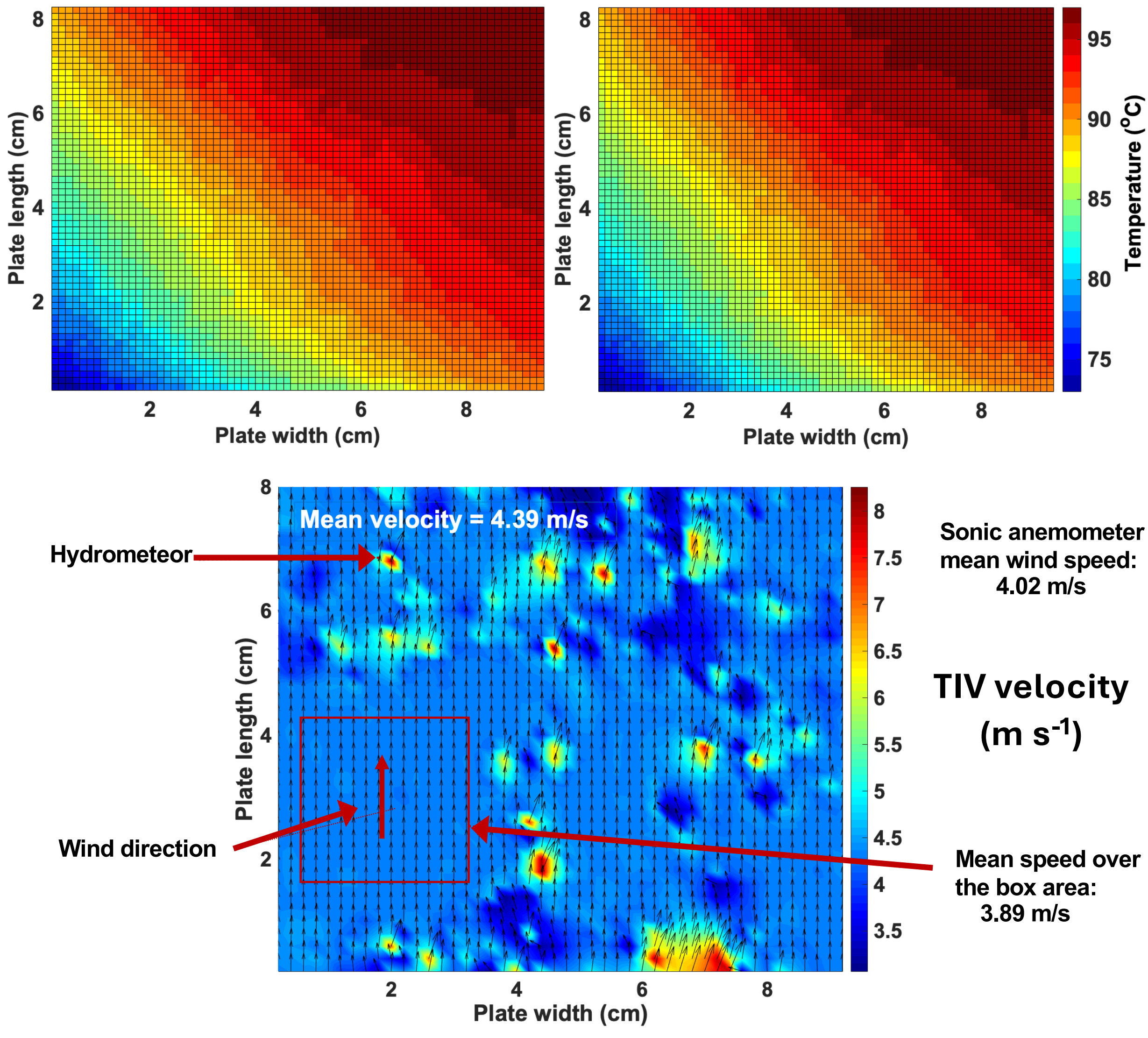

Figure 5. Lab demonstration of DTI-de capabilities to measuring both hydrometeors and horizontal wind components using Thermal Imaging Velocimetry (TIV). The top two figures show the propagation of temperature perturbations across the DTI-de during a 1-s interval seen with an infrared camera. Using TIV, hydrometeors on the DTI-de heated plate are clearly separable from wind vectors, which are obtained from the displacement of the temperature perturbation field. The advection velocity across the plate and can be correlated to the actual wind speed. The mean wind speed measured using TIV was 4.39 $\mathrm{m\,s^{-1}}$ compared to 4.02 $\mathrm{m\,s^{-1}}$ measured by a sonic anemometer in the wind tunnel.

https://doi.org/10.5194/egusphere-2026-3996
Preprint. Discussion started: 2 September 2026

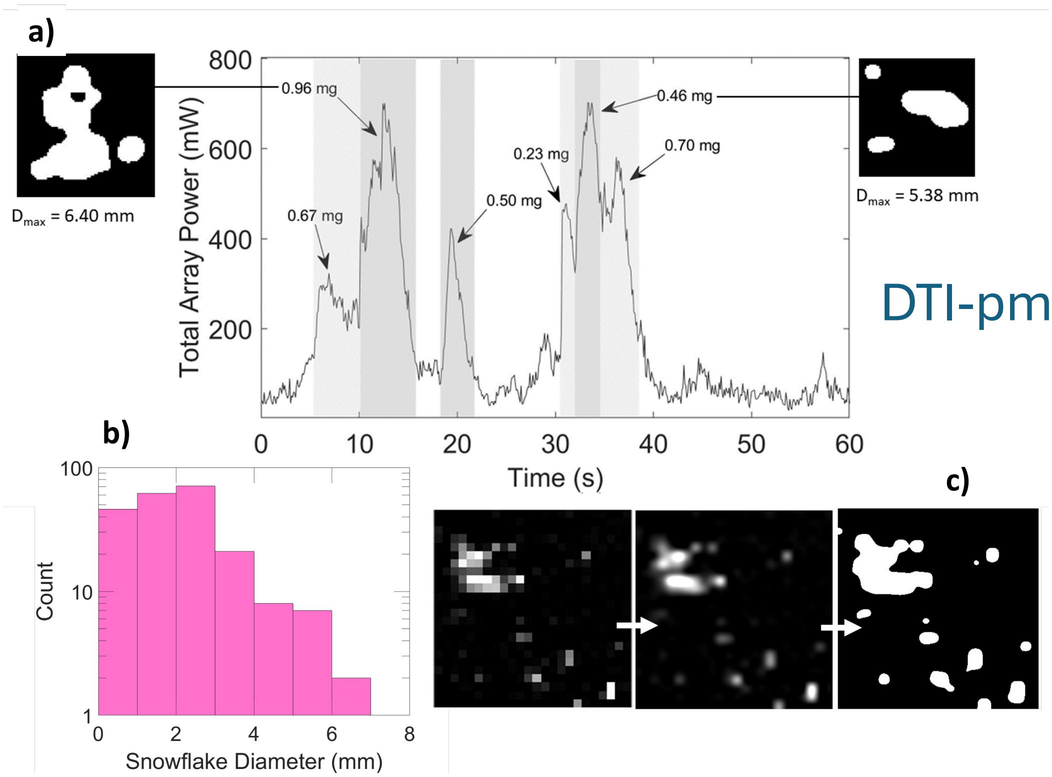

Figure 6. a) A time-series of DTI-pm data during snowy conditions at Alta on 19 April 2022. The shaded regions indicate snowflakes, with their associated masses labeled. b) A size distribution of snowflakes from Alta on a semi-log plot, exhibiting a negative exponential. c) Image processing used to resolve spatial dimensions.

a negative exponential consistent with expectations (Gunn and Marshall, 1958; Garrett, 2019). For this particular analysis, the thermodynamic image was binarized according to the per hotplate element power draw to identify the individual precipitation particle signature from which the particle geometric properties could be isolated, with the intermediate step that the native grid of the array DTI-pm micro-heater elements was linearly interpolated onto a finer grid.

A second DTI-pm device was situated on a Utah Department of Transport tower at Parley's Summit, a mountain pass at the top of Parley's Canyon with elevation 2,170 m, approximately 20 km east of Salt Lake City. It was placed alongside a Texas Electronics TE525WS tipping bucket-style precipitation gauge with a sensitivity of ∼2.5 mm/hr based on 5-minute averaging. Figure 7 shows a 24-hour time series of SWE rates from the two instruments showing how the DTI-pm produces similar measurements to the tipping bucket in heavier snowfall but with higher sensitivity.

With regards to the DTI-de, a comparison was made with SWE rates from the ETI Instrument Systems Noah II precipitation weighing gauge sensor and snow depth from the Campbell Scientific, Inc. SR50 ultrasonic snow depth sensor. The ETI and SR50 sensors were separated by 4 m from the DTI-de at the Alta site. A windshield was deployed around the ETI bucket to

https://doi.org/10.5194/egusphere-2026-3996
Preprint. Discussion started: 2 September 2026

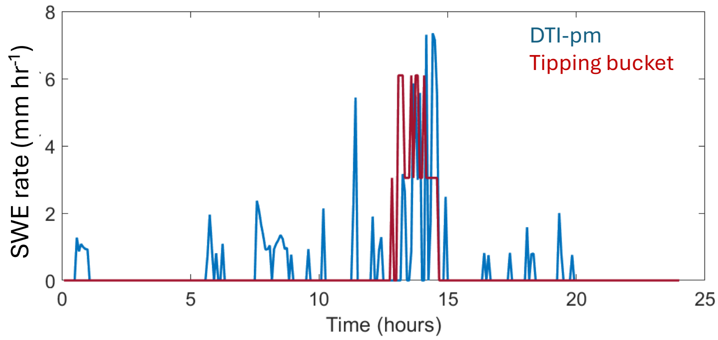

Figure 7. A 24-hour time series of SWE rates from the DTI-pm (blue) and a tipping bucket (red) during 24 February 2023 from Parley's Summit.

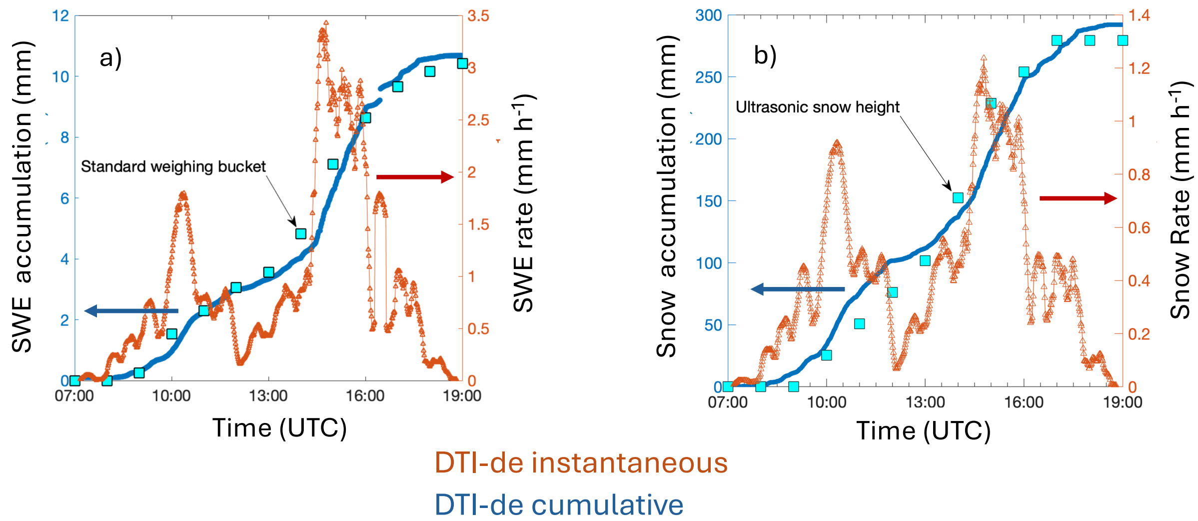

Figure 8. a) Time series of SWE accumulation and SWE rate measured using the DTI-de and an ETI gauge. Each DTI-de data point represents a 1 min average and each ETI gauge data point a 1h average. b) Time series of snow accumulation and snowfall rate measured using 1 min averaged DTI-de measurements and 1 h averaged ultrasonic snow depth sensor measurements during a storm on 12 December 2020 at Alta, Utah.

increase catchment efficiency. Manual snow depth and gravimetric weighing gauge measurements were also obtained once every 12 hours.

Figure 8a shows a comparison of the accumulated SWE integrated over 1 min intervals is compared to hourly ETI data in . Over a 12 h period during the storm, DTI-de SWE and ETI gauge accumulations agree to within ±6%. The ETI accumulation is slightly lower, perhaps because the ETI resolution is 0.25 mm compared with 0.001 mm for the DTI-de, and also because the

https://doi.org/10.5194/egusphere-2026-3996
Preprint. Discussion started: 2 September 2026

ETI is subject to undercatch during high winds (Singh et al., 2021). Figure 8b shows snow accumulations inferred from ratio of SWE measurements and estimates of snow density obtained by the DTI-de, showing good agreement to within ±5 % with hourly measurements of snowpack depth from an ultrasonic snow depth sensor.

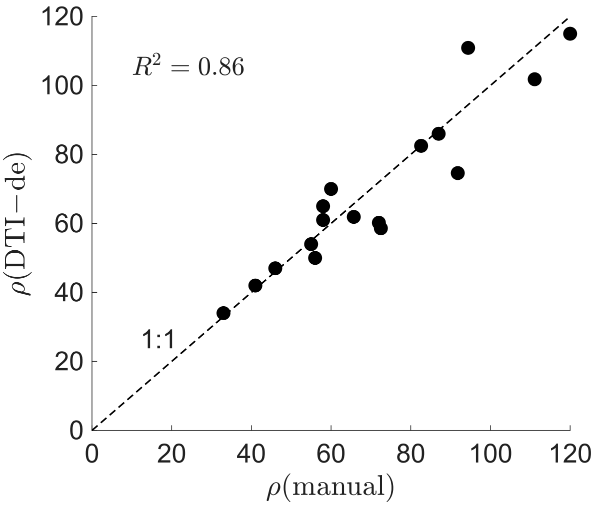

Figure 9. Continuous DTI-de measurements of snowflake density compared with ETI SR50 manual measurements obtained twice daily averaged over 17 storms during the 2020-2021 winter season during which approximately 1300 cm of snow fell, with ambient temperatures ranging from $-22°$C to $-2°$C.

During the 2020–2021 winter season, the Alta site received approximately 1300 cm of snowfall, with ambient temperatures ranging from $-22°$C to $-2°$C. Density measurements from the DTI-de averaged over 17 storms during the season are shown in Figure 9, compared with manual measurements obtained at 12-h intervals (Singh et al., 2024). For the manual measurements, total SWE and total snow depth H were measured over each 12-h interval. Bulk snow density was estimated from $\rho = \rho_w \,\mathrm{SWE}/H$, where ρ_w is the bulk density of liquid water. Compared to a 1:1 line, the R^2 value relating the two measurements is 0.86. The degree to which continuous DTI-de and manual measurements agree is somewhat surprising given the DTI-de measurements are derived from the integrated properties of individual snowflakes as they land on the plate, and that no account is made for how they pack and stack in the snow pack.

At the same location on 6 January 2023, during which ambient temperatures varied from -5 to -7°C, the DTI-pm and DTI-de were collocated for comparison, separated horizontally by ∼1 m, and raised ∼1.5 m above the new snow surface. Figure 10 shows a comparison of instantaneous and cumulative precipitation measured by both devices for a period when the DTI-de measured 31.2 mm of SWE and the DTI-pm 30.4 mm of SWE, a difference of 2.6%.

Over the 2023-2024 boreal winter season, a DTI-de unit was installed at a second site in Alta, Utah at the Atwater Snow Study Plot in Alta, Utah. The study plot contained a variety of meteorological and snow study equipment, including approximately 3 m away the OTT Parsivel^2 disdrometer(Löffler-Mang and Joss, 2000). Figure 11 shows a comparison of snowflake size distributions observed by the DTI-de and Parsivel^2 for a two day period between 16 UTC January 2, 2024 and 16 UTC

https://doi.org/10.5194/egusphere-2026-3996
Preprint. Discussion started: 2 September 2026

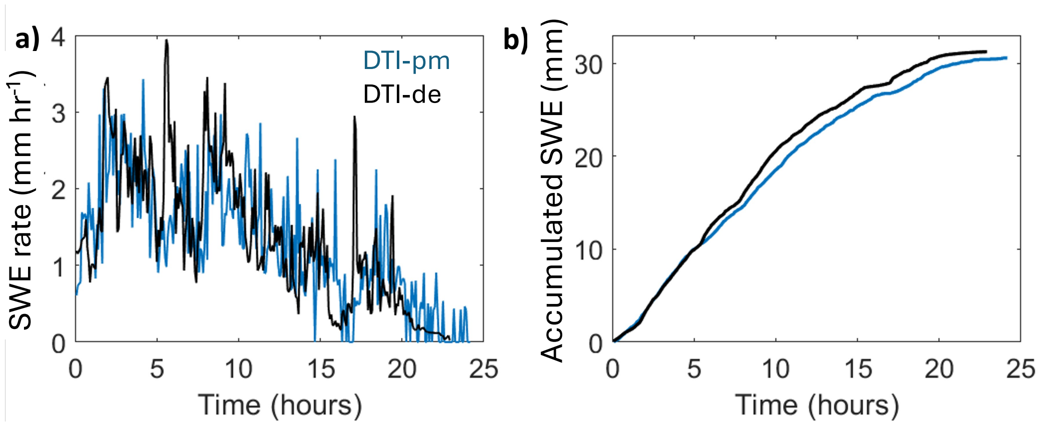

Figure 10. 24-hour time series from 6 January 2023 of a) SWE rate measured by the DTI-pm (blue) and DTI-de (black) and b) accumulated SWE from the DTI-pm (blue) and DTI-de (black).

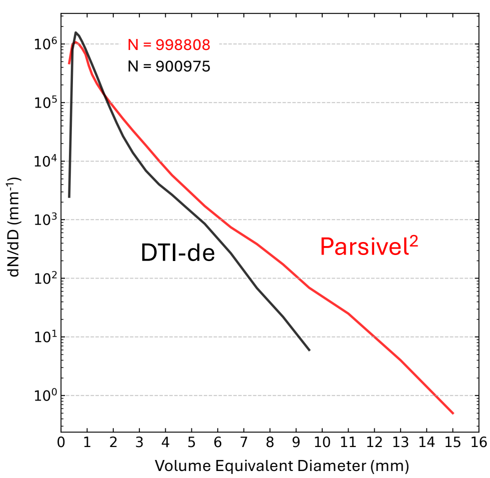

Figure 11. Comparison of snow size distributions from the DTI-de (black) and the Parsivel^2 (red) obtained during light winds with a mean speed of $1.5\,\mathrm{m\,s^{-1}}$. The ambient temperature ranged from $-13°\mathrm{C}$ to $-3°\mathrm{C}$, with a mean of $-9°\mathrm{C}$.

January 4, 2024 with a mean temperature of -9° C. Approximately one million hydrometeors were sampled by each device. The size parameter from the Parsivel^2 is the equivalent sphere diameter and does not have a direct microphysical analog. It is derived from the shadowed area of the Parsivel^2 laser sheet and is based on an assumption that the particles are uniform liquid spheroids with an axial ratio that varies linearly as a function of the equivalent volume sphere diameter D_v (Battaglia et al., 2010). The comparison made here is between the Parsivel^2 value of D_v and values of D_v inferred from direct DTI-de measurements of individual hydrometeor mass assuming the density of liquid water. The mode of the size distribution is similar

https://doi.org/10.5194/egusphere-2026-3996
Preprint. Discussion started: 2 September 2026

for both instruments, located at approximately 0.6 mm, with a modest shift to smaller sizes for the Parsivel^2. However, there are substantial differences in the sizing of larger particles. The reason is unknown, but there is no direct means to obtain a liquid D_v for snowflakes from the Parsivel^2 without assuming a snowflake density. No such assumption is required for the DTI-de.

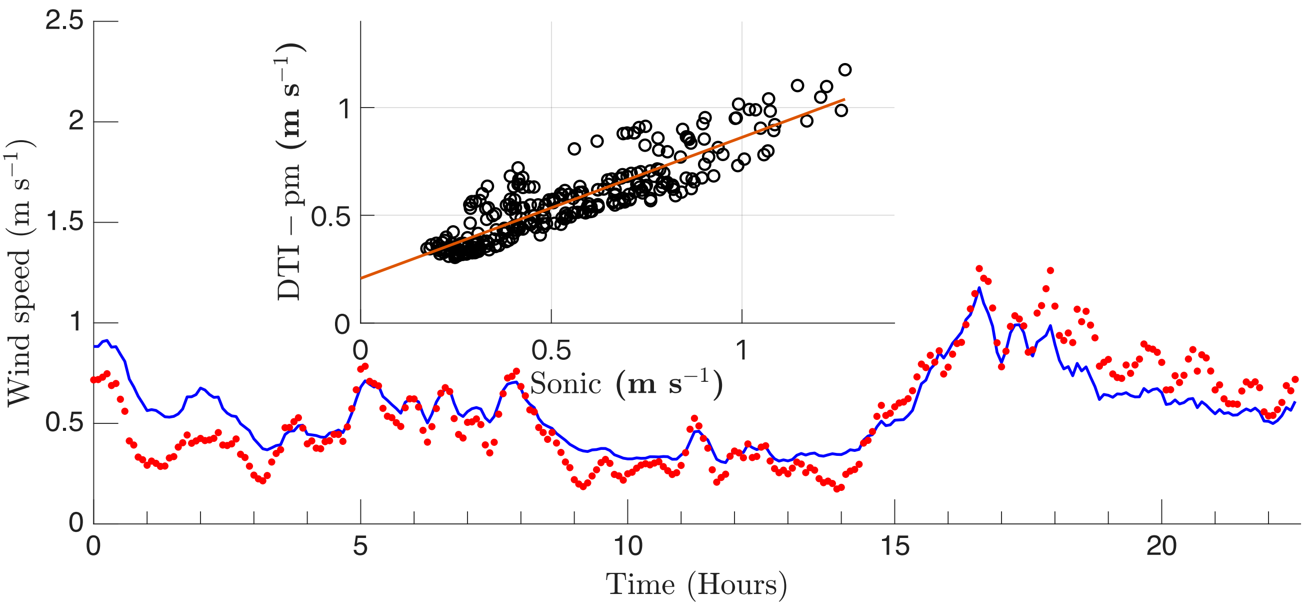

Figure 12. Measurements of wind speeds obtained by the DTI-pm and a Campbell Scientific 3D sonic anemometer averaged over 5 minute intervals. The inset shows a scatter plot of the two datasets in the time series, indicating a coefficient of 0.65 and and an intercept of 0.21 $\mathrm{m\,s^{-1}}$ with an R^2 value of 0.78.

The application of the DTI principles to wind measurement has thus far only been explored in a field context for the DTI-pm. Figure 12 shows a comparison between measurements of light winds obtained by the DTI-pm and a Campbell Scientific 3D sonic anemometer separated by $\sim 1\,\mathrm{m}$ horizontally and located at a site on the campus of the University of Utah. DTI-pm measurements of wind speed were inferred based on the $Re(Nu)$ relationship given by Eq. 4. Measurements of the winds from the two devices indicate both have the capability of measuring very light winds, and that both devices covary with a high coefficient of determination of $R^2 = 0.78$. Nonetheless, there are differences. The coefficient relating the DTI-pm wind speed to the sonic anemometer wind speeds is 0.65 with an intercept of 0.21 $\mathrm{m\,s^{-1}}$.

5 Conclusions

Accurate, sensitive precipitation measurement remains a substantial challenge using tipping-bucket, weighing-gauge, or optical-probes, especially when it is frozen. Precipitation hotplates have advantages for frozen precipitation because they are less prone to collection inefficiencies and their measurement method is based on the first-principles thermodynamics of how much energy

https://doi.org/10.5194/egusphere-2026-3996
Preprint. Discussion started: 2 September 2026

is required to evaporate a precipitation particle. However, previous hotplate designs have suffered from unresolved environmental influences on the signal and only provided single point measurements.

We introduced here a new automated hotplate concept based on discrete thermal imaging (DTI) that permits first principles information to be obtained of precipitation bulk and microphysical properties based on the spatial and temporal mapping of power losses from the plate that are forced by atmospheric thermodynamic signatures. Two devices are described. The DTI-pm is manufactured from an array of micro-hotplates and uses pulse-width modulation to maintain each element at a constant temperature against power losses. The DTI-de exploits the difference in emissivity of water and metal in thermal imagery of precipitation particles on a heated metal plate, and surface temperature maps to quantify precipitation mass, density, and size distributions. While the DTI-pm requires greater complexity in manufacture than the DTI-de, it does not require camera calibration, nor does it require occasional cleaning of dust and salt contamination that appears in the infrared imagery. Laboratory and field measurements demonstrate a capacity of the DTI principle to measure the density, mass, and size of individual hydrometeors, as well as the bulk, integrated properties of precipitation amount and, in the case of frozen precipitation, snow depth. We find that both devices demonstrate higher sensitivity and accuracy than existing standard precipitation and snowpack measurement technologies.

The DTI concept is undergoing further testing and development, in particular with regards to laboratory and field experiments that demonstrate a potential to concurrently measure precipitation, wind speed, and direction. Because the DTI is a generalized thermodynamic sensor, the potential is for it to measure a wide range of meteorological variables from signal processing applied to a single technique. It may be possible to adapt and extend this technology to a comprehensive weather sensor, as all atmospheric signals are fundamentally thermodynamic, and therefore measurable using the DTI principle.

Author contributions. T.J.G contributed to experiment design and setup,and writing and editing of the manuscript. R.S. contributed to the experiment design and setup, data collection and analysis, and writing of the manuscript. E.R.P contributed to experiment design and setup, and editing of the manuscript. D.K.S. contributed to the experiment design and setup, data collection, and analysis. A.T.R contributed to experiment design and setup, and data collection and management. B.H.S. contributed to the experiment design and setup, data collection, and analysis. K.N.R. contributed to the experiment design and setup, and data collection and analysis. A.B. contributed to data analysis. In addition, T.J.G. and E.R.P. and A.T.R. acted as project leads.

Data availability. Data that support the findings of this study are available from https://hive.utah.edu/records/nxsf5-z6814

.

https://doi.org/10.5194/egusphere-2026-3996
Preprint. Discussion started: 2 September 2026

Competing interests. Conflict of interest: The DTI-de and DTI-de technologies are protected through US patents 11674878 and 11640013 including authors D.K.S., E.R.P., and T.J.G.. They are commercially available through Particle Flux Analytics, Inc. (PFA) of which A.T.R and T.J.G. are co-founders. PFA has a license from the University of Utah to commercialize DTI technologies.

Acknowledgements. We thank Steven Clark of the Utah Department of Transportation (UDOT), and Dave Richards and Johnathan Morgan of the Alta Ski Patrol for field support, Allan Reaburn and colleagues at Particle Flux Analytics, Inc. for helping to lead the development and advancement of the DTI-de and DTI-pm. Particle Flux Analytics, Inc. owns invention and process licenses, proprietary data rights for the DTI-de and DTI-pm principles under the respective trademarks DEID™and SnowPixel™.

Financial support. DTI development is based upon work supported by the U.S. Department of Energy through SBIR Awards granted to Particle Flux Analytics, Inc. under contract numbers DE-SC0017168, DE-SC0022516, and DE-SC0025812, and the U.S. National Science Foundation to the University of Utah through grants PDM-1841870 and PDM-2210179.

References

Ahmad, T., Binder, S., Leber, M., Reiche, C. F., Solzbacher, F., and Garret, T. J.: Fabrication of polymer membrane-suspended microstructures on printed circuit boards, J. Microelectromechanical Sys., 2022.

Battaglia, A., Rustemeier, E., Tokay, A., Blahak, U., and Simmer, C.: PARSIVEL Snow Observations: A Critical Assessment, J. Atmos. Oceanic Technol., 27, 333–344, https://doi.org/10.1175/2009JTECHA1332.1, 2010.

Bergman, T. L., Lavine, A. S., Incropera, F. P., and DeWitt, D. P.: Introduction to heat transfer, John Wiley & Sons, 2011.

Biswas, A. K.: The automatic rain-gauge of Sir Christopher Wren, FR S, Notes and Records of the Royal Society of London, 22, 94–104, 1967.

Cauteruccio, A., Colli, M., Stagnaro, M., Lanza, L. G., and Vuerich, E.: In-situ precipitation measurements, in: Springer Handbook of Atmospheric Measurements, pp. 359–400, Springer, 2021.

Chinchella, E., Cauteruccio, A., and Lanza, L. G.: Impact of Wind on Rainfall Measurements Obtained from the OTT Parsivel2 Disdrometer, Sensors, 25, https://doi.org/10.3390/s25206440, 2025.

Ficklin, D. L., Null, S. E., Abatzoglou, J. T., Novick, K. A., and Myers, D. T.: Hydrological intensification will increase the complexity of water resource management, Earth's Future, 10, e2021EF002 487, 2022.

Foss, J. F., Bohl, D. G., and Hicks, T. J.: The pulse width modulated constant temperature anemometer, Measurement Science and Technology, 7, 1389–1396, https://doi.org/10.1088/0957-0233/7/10/006, 1996.

Garrett, T. J.: Analytical Solutions for Precipitation Size Distributions at Steady State, J. Atmos. Sci., 76, 1031–1037, 2019.

Goodison, B. E., Louie, P. Y., and Yang, D.: WMO solid precipitation measurement intercomparison, 1998.

Gunn, K. L. S. and Marshall, J. S.: THE DISTRIBUTION WITH SIZE OF AGGREGATE SNOWFLAKES, Journal of Meteorology, 15, 452–461, https://doi.org/10.1175/1520-0469(1958)015<0452:TDWSOA>2.0.CO;2, 1958.

Hobbs, P. V. and Rangno, A. L.: Atmospheric Science-L13102 Super-large raindrops (DOI 10.1029/2004GL020167), Geophysical Research Letters, 31, 2004.

Huntington, T. G.: Climate warming-induced intensification of the hydrologic cycle: an assessment of the published record and potential impacts on agriculture, Advances in agronomy, 109, 1–53, 2010.

Incropera, F., DeWitt, D., Bergman, T., and Lavine, A.: Fundamentals of Heat and Mass Transfer, Wiley, https://books.google.com/books?id=vvyIoXEywMoC, 2011.

Jevons, W. S.: LIV. On the deficiency of rain in an elevated rain-gauge, as caused by wind, The London, Edinburgh, and Dublin Philosophical Magazine and Journal of Science, 22, 421–433, https://doi.org/10.1080/14786446108643180, 1861.

Johannsen, L., Zambon, N., Strauss, P., Dostal, T., Neumann, M., Zumr, D., Cochrane, T., Blöschl, G., and Klik, A.: Comparison of three types of laser optical disdrometers under natural rainfall conditions, Hydrological Sciences Journal, 65, 524–535, https://doi.org/10.1080/02626667.2019.1709641, 2020.

Kidd, C., Becker, A., Huffman, G. J., Muller, C. L., Joe, P., Skofronick-Jackson, G., and Kirschbaum, D. B.: So, How Much of the Earth's Surface Is Covered by Rain Gauges?, Bulletin of the American Meteorological Society, 98, 69 – 78, https://doi.org/10.1175/BAMS-D-14-00283.1, 2017.

Kirchmeier-Young, M. C. and Zhang, X.: Human influence has intensified extreme precipitation in North America, Proceedings of the National Academy of Sciences, 117, 13 308–13 313, 2020.

https://doi.org/10.5194/egusphere-2026-3996
Preprint. Discussion started: 2 September 2026

Lance, S.: Coincidence Errors in a Cloud Droplet Probe (CDP) and a Cloud and Aerosol Spectrometer (CAS), and the Improved Performance of a Modified CDP, Journal of Atmospheric and Oceanic Technology, 29, 1532 – 1541, https://doi.org/10.1175/JTECH-D-11-00208.1, 2012.

Löffler-Mang, M. and Joss, J.: An optical disdrometer for measuring size and velocity of hydrometeors., J. Atmos. Ocean. Tech., 17, 130–139, 2000.

Löffler-Mang, M., Kunz, M., and Schmid, W.: On the performance of a low-cost K-band doppler radar for quantitative rain measurements, J. Atmos. and Ocean. Tech., 16, 379–387, https://doi.org/10.1175/1520-0426(1999)016<0379:OTPOAL>2.0.CO;2, 1999.

Morrison, T. J., Meisenheimer, T., Garrett, T., Singh, D., Donovan, S., and Pardyjak, E.: Relating storm-snow avalanche instabilities to data collected from the Differential Emissivity Imaging Disdrometer (DEID), Cold Regions Science and Technology, 210, 103 839, 2023.

Nanditha, J. S., Kushwaha, A. P., Singh, R., Malik, I., Solanki, H., Chuphal, D. S., Dangar, S., Mahto, S. S., Vegad, U., and Mishra, V.: The Pakistan Flood of August 2022: Causes and Implications, Earth's Future, 11, e2022EF003 230, https://doi.org/https://doi.org/10.1029/2022EF003230, e2022EF003230 2022EF003230, 2023.

Raffel, M., Willert, C. E., and Kompenhans, J.: Particle image velocimetry: a practical guide, Springer, 1998.

Rasmussen, R. M., Hallett, J., Purcell, R., Landolt, S. D., and Cole, J.: The hotplate precipitation gauge, Journal of Atmospheric and Oceanic Technology, 28, 148–164, 2011.

Rees, K. N., Singh, D. K., Pardyjak, E. R., and Garrett, T. J.: Mass and density of individual frozen hydrometeors, Atmospheric Chemistry and Physics, 21, 14 235–14 250, https://doi.org/10.5194/acp-21-14235-2021, 2021.

Singh, D. K., Donovan, S., Pardyjak, E. R., and Garrett, T. J.: A differential emissivity imaging technique for measuring hydrometeor mass and type, Atmos. Meas. Tech., 14, 6973–6990, https://doi.org/10.5194/amt-14-6973-2021, 2021.

Singh, D. K., Pardyjak, E. R., and Garrett, T. J.: Time-resolved measurements of the densities of individual frozen hydrometeors and fresh snowfall, Atmospheric Measurement Techniques, 17, 4581–4598, https://doi.org/10.5194/amt-17-4581-2024, 2024.

Stickel, J., Maloney, B., Pape, C., and Burkheimer, D.: Evaluation of the hotplate snow gauge, Aurora Project 2004-01, Tech. rep., Aurora, http://aurora-program.org, 2005.

Tapiador, F. J., Turk, F., Petersen, W., Hou, A. Y., García-Ortega, E., Machado, L. A., Angelis, C. F., Salio, P., Kidd, C., Huffman, G. J., and de Castro, M.: Global precipitation measurement: Methods, datasets and applications, Atmospheric Research, 104-105, 70–97, https://doi.org/https://doi.org/10.1016/j.atmosres.2011.10.021, 2012.

Thériault, J. M., Leroux, N. R., and Rasmussen, R.: Improvement of solid precipitation measurements using a hotplate precipitation gauge, Journal of Hydrometeorology, https://doi.org/10.1175/JHM-D-20-0168.1, 2021.

Thériault, J. M., Rasmussen, R., Ikeda, K., and Landolt, S.: Dependence of Snow Gauge Collection Efficiency on Snowflake Characteristics, Journal of Applied Meteorology and Climatology, 51, 745 – 762, https://doi.org/10.1175/JAMC-D-11-0116.1, 2012.

Villermaux, E. and Bossa, B.: Single-drop fragmentation determines size distribution of raindrops, Nature Physics, 5, 697, https://doi.org/10.1038/nphys1340, 2009.

Çengel, Y. A. and Ghajar, A. J.: Heat and Mass Transfer: Fundamentals and Applications, McGraw-Hill, 2015.